Eng. Sci., 2021, **14**, 27–38

Engineered Science

DOI: https://dx.doi.org/10.30919/es8d1311

NH_3-activated Fullerene Derivative Hierarchical Microstructures to Porous Fe_3O_4/N-C for Oxygen Reduction Reaction and Zn-air Battery

Zhiyao Peng,[1] Qinglong Jiang,[2] Ping Peng[1,*] and Fangfang Li[1,*]

Abstract

Development of high-performance oxygen reduction reaction (ORR) catalysts to replace the noble metal-based materials is critical for energy applications. Fullerenes, in the form of carbon cage with the intrinsic curvature and pentagons, have been theoretically simulated as promising ORR catalysts via atom doping and defect modification. However, fullerene-based catalysts remain challenging in achieving ORR performance comparable to Pt/C given the lack of fullerene host-dopant synergism. A rational strategy is to anchor active species on fullerene cage to enhance ORR response. Herein, a Fe, N-decorated fullerene derivative (*N*-methyl-2-ferrocenyl-pyrrolidinofullerene C_{60}) is activated under NH_3 stream to achieving porous Fe_3O_4/N-C nanomaterials with high catalytic activity toward ORR. The optimal NH_3-etching temperature of 700 °C gives rise to open-pore structures, large surface area, favorable N doping, active Fe_3O_4 sites and short-range ordered nanographene. Through these synergetic effects, the fullerene-derived FMN700 exhibits superior ORR activity, along with respectable durability and tolerance to methanol, which surpass most of the reported fullerene-based carbon materials. This work provides a new strategy for the design and synthesis of porous carbon composites as a new class of catalysts for high-performance ORR.

Keywords: Fullerene derivative; Hierarchical microstructure; NH_3-activation; Oxygen reduction reaction; Zinc-air battery.
Received: 1 January 2021; Accepted: 16 January 2021.
Article type: Research article.

1. Introduction

Propelled by the aggravating fossil energy crisis, considerable efforts have been invested in renewable energy sources such as metal-air batteries and fuel cells. However, the cathodic oxygen reduction reaction (ORR) restricts the holistic efficiency due to the kinetically sluggish reaction and excessive overpotential.[1-3] Precious metal platinum shows the highest kinetic activity in the ORR catalysis, whereas its large-scale commercial use is impeded by the high cost, inferior long-term stability and methanol tolerance.[4-8] Alternatively, porous carbon structures with defects (such as holes, pentagons and edges) and/or doped heteroatoms,[9-14] and transition metal/N-C series[15-19] have been demonstrated to be ORR active in view of the synergetic effects between the conductive carbon matrix and the abundant reactive sites. However, the synthesis of heteroatom and metal-doped porous carbon structures is very complicated, requiring multiple precursors, templates, additional processes such as activation and acid etching.[20-24] Thus, it is important to explore new strategies to facilely synthesizing porous nanocarbons composites.

Fullerene carbon cage, featuring π-conjugated curved surface with the intrinsic pentagon defects has attracted great attention in renewable energy field in recent years.[25,26] Hybrid density functional theory (DFT) calculations have indicated that (i) the curvature and pentagon rings of fullerenes can promote the catalytic activity toward ORR because the active sites are associated with the adjacent pentagons, and (ii) defected fullerene molecules resulted from heteroatoms decoration were realized as promising catalysts in ORR since the O_2 molecule can be effectively chemisorbed, activated and reduced on heteroatom doped C_{60}.[27-31] Some interesting results about the design and synthesis of fullerene-based

[1] *State Key Laboratory of Materials Processing and Die & Mould Technology, School of Materials Science and Engineering, Huazhong University of Science and Technology, Wuhan 430074, China.*

[2] *Department of Chemistry and Physics, University of Arkansas, Pine Bluff, AR 71601, USA.*

**E-mail:* ppeng@hust.edu.cn (P. Peng), ffli@hust.edu.cn (F. F. Li)

materials for ORR have been reported recently. For example, Mu and co-workers opened the pristine C_{60} molecule through KOH activation and the obtained pentagon-rich graphitic carbon was proved to enhance the ORR performance.[32] Fullerene modified graphene synthesized by Yang's group exhibited improved ORR catalytic activity than the pristine graphite.[33] Lu *et al*. prepared the 2D high-surface-area mesoporous carbon from fullerene microsheets, which was examined as an effective ORR catalyst.[34] Vinu and co-workers fabricated two highly ordered mesoporous carbon materials from C_{60}[35] and C_{70},[36] respectively for high performance ORR. Moreover, anchor of Cu-Cu_2O nanoparticles on a mesoporous fullerene improved the onset potential by 40 mV compared with the mesoporous fullerenes.[37] Although fullerene-based materials have been realized active for oxygen reduction, it remains challenging in achieving ORR performances comparable to Pt/C due to the lack of fullerene host-dopant synergism. To surmount these issues, we can add active species to the surface of fullerene through covalent bonds to prepare fullerene derivatives, so as to achieve the fullerene host-dopant synergistic effect and boost the ORR. As well known, fullerene can be modified at the molecular level with desired functional groups, providing the opportunity to effectively tune the catalytic properties of the derived materials. However, the utilization of fullerene derivatives to prepare active materials for ORR and zinc-air battery has never been studied.

Herein, a fullerene derivative, *N*-methyl-2-ferrocenyl-pyrrolidinofullerene C_{60} (denoted as Fc-C_{60}) with a pyrrolidine and a ferrocene group, was utilized as a precursor to achieve in situ N and Fe dual-doped active carbon material. Fc-C_{60} molecules were firstly self-assembled into a 3D highly ordered hierarchical microstructure through the template-free liquid-liquid interface precipitation (LLIP) method. Thermal treatment of the 3D hierarchical microstructure at 600, 700 and 800 °C under an NH_3 atmosphere resulted in a series of N, Fe co-doped 3D porous carbon materials (named as FMN600, FMN700 and FMN800, respectively). The FMN700 sample features a unique carbon framework with hierarchically dispersed pore structures, favorable N doping and active Fe_3O_4 nanoparticles uniformly embedded on the short-range ordered nanographene, and exhibits high performance for ORR with the onset potential (E_{on}) of 0.93 V and the half-wave potential ($E_{1/2}$) of 0.81 V vs. RHE, which surpassed those of the most reported fullerene-based ORR electrocatalysts. It also shows excellent long-term durability and high tolerance to methanol, outperforming the commercialized Pt/C catalyst. Further examination of FMN700 in Zn-air battery demonstrated activity comparable to the Pt/C and much higher activity than the C_{60}-based carbons. The current work not only demonstrates the pyrolysis behavior of the fullerene hierarchical microstructures under NH_3, but also develops a new strategy for preparing new high-performance ORR catalysts. By introducing various functional groups on the fullerene cage, many new carbon structures could be developed.

2. Experimental section

2.1 Materials

Fullerene (C_{60}) and ferrocene were purchased from commercial sources without further purification. Potassium hydroxide (KOH), isopropyl benzene (IPB), chlorobenzene (CB), and ethanol (EA) are all available from Titan, Ltd. Nafion (0.5 wt%) was purchased from Alfa Aesar and used as received.

2.2 Preparation of Fc-C_{60} (FP)

The preparation and purification of *N*-methyl-2-ferrocenyl-pyrrolidinofullerene C_{60} (Fc-C_{60}) were proceeded according to a previous work.[38]

2.3 Preparation of Fc-C_{60} microstructures (FM)

Fc-C_{60} microstructures were prepared through a template-free liquid-liquid interfacial precipitation (LLIP) method in which the combined isopropyl benzene (IPB) and chlorobenzene (CB) were selected as good solvents and ethanol as a poor solvent, respectively. Typically, Fc-C_{60} (15 mg) was dissolved in the mixed solvents of 10 mL IPB and 10 mL CB by ultrasonic dispersion, which was filtered twice to prepare a clear solution. Then the solution was injected slowly into EA (60 mL). The obtained solution was aged for 12 h. Finally, the precipitation on the bottom was collected by centrifuge at 6000 rpm and vacuum dried at 40 °C overnight.

2.4 Preparation of FMN600/700/800, FMA700 and FPN700

The obtained Fc-C_{60}microstructures were heated at 600, 700 and 800 °C, respectively under the NH_3 stream and held for 3 h to yield black powders of FMN600/700/800. For comparison, FMA700 was synthesized by heating the Fc-C_{60} microstructure (FM) at 700 °C under Ar stream for 3h. FPN700 was prepared by thermal treatment of Fc-C_{60} powder (FP) at 700 °C under the NH_3 for 3h. The rate of heating is 5 °C min^{-1} and the gas flow rate is 60 mL min^{-1} for all the experiments.

2.5 Characterizations

Scanning Electron Microscopy (SEM) images was obtained on a FEI Nova Nova NanoSEM 450 Scanning Electron Microscope. Transmission Electron Microscopy (TEM), High Resolution Transmission Electron Microscopy (HRTEM) and High-Angle Annular Dark Field Scanning Transmission Electron Microscopy (HAADF-STEM) were acquired on a Talos F200X. N_2 adsorption/desorption isotherms were measured on a Micromeritics TriStar II 3flex analyzer. X-ray diffraction (XRD) patterns and Raman spectra were obtained at an Empyrean powder X-ray diffractometer with Cu target and a Bruker VERTEX 70 research spectrometer, respectively. The interlayer spacing d is calculated by Bragg's equation, $2d\sin\theta = n\lambda$, where n is a positive integer (n = 1) and λ

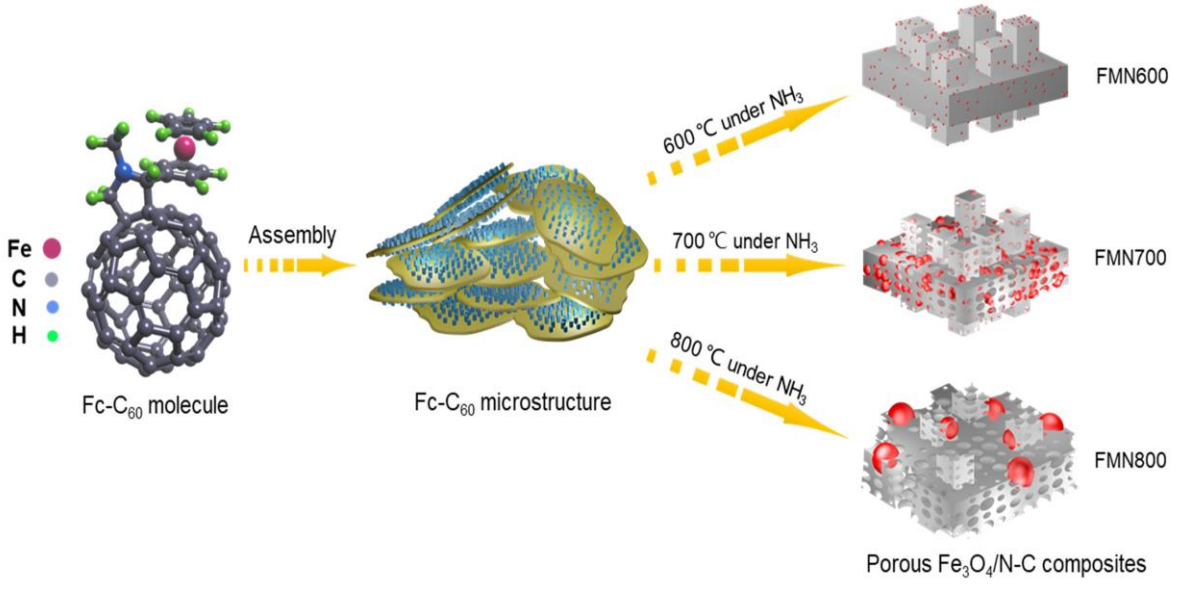

Scheme 1 Preparation processes of N-methyl-2-ferrocenyl-pyrrolidinofullerene C_{60} nanoarray architecture via a template-free LLIP method, and the 3D N,Fe-co-doped carbon composites through annealing under the NH_3 stream

(0.15406 nm) is the incident X-ray wavelength of. X-ray photoelectron spectrometer (XPS) was carried out on a AXIS-ULTRA DLD-600W, Kratos.

2.6 Electrochemical Measurements

All electrochemical tests were performed on a CHI760E electrochemical workstation in a conventional three-electrode system at 25 °C. A rotating ring-disk electrode (RRDE) with a glass carbon (GC) disk of 5 mm diameter was used as the working electrode. A graphite rod and a saturated calomel electrode (SCE) electrode were used as the counter and reference electrodes, respectively. All the potential-related data recorded in this work were calibrated with respect to the reversible hydrogen electrode (RHE). To prepare the catalyst ink, 5 mg of active catalyst powder and 40 µL of 5 wt% Nafion solutions were dispersed in 480 µL ethanol and 480 µL water with the assistance of ultrasonication for at least 40 min. The loading mass of catalysts was kept at 0.1 mg cm^{-2} for Pt/C and 0.5 mg cm^{-2} for the other catalysts. The disk rotation rate is 1600 rpm unless specifically mentioned. The electrocatalytic activity of the obtained samples towards the ORR was investigated by the line sweep voltammetry (LSV) and cyclic voltammetry (CV) techniques with a scan rate of 10 mV s^{-1}. The durability and methanol crossover tests for the ORR activity were performed by chronoamperometry (CA) at 0.6 V vs. RHE. The apparent number of electrons transferred during ORR on the carbon catalysts was determined by the Koutechy-Levich equation given by:

$$\frac{1}{J} = \frac{1}{J_L} + \frac{1}{J_K} = \frac{1}{B\omega^{\frac{1}{2}}} + \frac{1}{J_K} \quad (1)$$

$$B = 0.62nFC_0D_0^{\frac{2}{3}}V^{-\frac{1}{6}} \quad (2)$$

where J is the measured current density, J_K and J_L are the kinetic and limiting current densities, ω is the angular velocity of the disk (between 400 to 2500 rpm), n is the overall number of electrons transferred in oxygen reduction, F is the Faraday constant (96485 C mol^{-1}), C_0 is the bulk concentration of O_2 (1.1×10^{-6} mol cm^{-3}), D_0 is the diffusion coefficient of O_2 in 0.1 mol L^{-1} (M) KOH (1.9×10^{-5} cm^2 s^{-1}), and V is the kinematic viscosity of the electrolyte (0.01 cm^2 s^{-1}).

2.7 Zn-air battery tests

Zn-air battery tests were performed in a customized electrochemical cell using 6 M KOH as an electrolyte and the zinc foil as an anode. The air cathode was prepared by uniformly coating the catalyst ink (2 mg cm^{-2}) on a hydrophobic carbon paper. A Celgard 2340 microporous membrane soaked with 6 M KOH electrolyte was employed as the separator. All Zn-air batteries were assembled and tested under ambient conditions. The polarization curves were obtained by linear sweep voltammetry at 10 mV s^{-1} and the galvanostatic discharge curves were recorded at 10 mA cm^{-2} on a CHI760E electrochemical workstation.

3. Results and discussion

Ordered fullerene crystalline microstructures have been proved to be important to enhance the performance in energy applications.[35,36,39-41] Thus, the fullerene derivative, *N*-methyl-2-ferrocenyl-pyrrolidinofullerene C_{60} (Fc-C_{60}) was firstly assembled into the 3D hierarchical microstructures by LLIP process, in which the cuboids were anchored on the microplates (see Scheme. 1 and the details in the Experimental Section). Although the growth mechanism is not yet clear, the structural advantage of the 1D cuboids growth can be established by separating the 2D microplates with each other, providing the necessary interval for NH_3 infiltration and increasing the surface area. To remove the air before the subsequent annealing process, the quartz tube was filled with Argon (Ar) after the evacuation of air and then was refilled

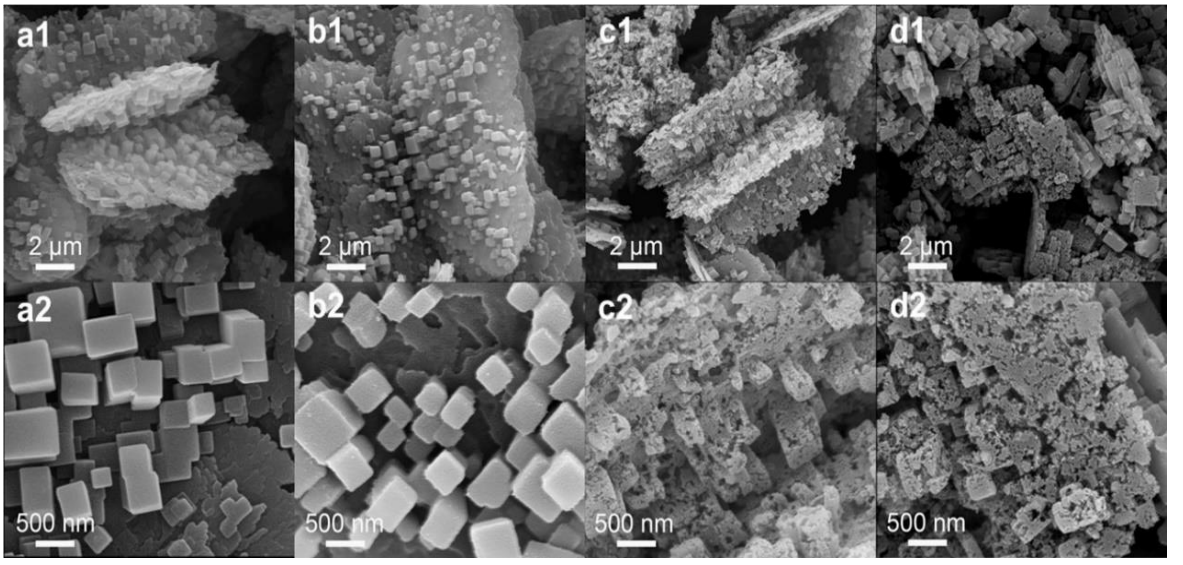

Fig. 1 FESEM images of FM (a1, a2), FMN600 (b1, b2), FMN700 (c1, c2) and FMN800 (d1, d2).

with the NH_3 after the evacuation of Ar. After heating at 600, 700 and 800 °C under the NH_3 stream, three 3D hierarchical porous nanocarbon structures (FMN600/700/800) were obtained. The NH_3 treatment outstands for several advantages including pore opening,[42] introduction of different N groups[43,44] and improvement of graphitic degree of carbon matrix.[45]

Field emission scanning electron microscopy (FESEM) was employed to identify the morphologies of the samples before and after the heat treatment in Fig. 1 and Fig. S1-S3. Compared to the Fc-C_{60} powder (FP) (Fig. S1), the crystalline Fc-C_{60} microstructure (FM) (Fig. 1a and Fig. S2a) obtained through the LLIP process presents a hierarchical growth pattern with cuboids growing on the microplates, which can expand the surface area for electrochemical reactions. After annealing under the NH_3 at 600 °C, the microstructure of the FMN600 was found intact, whereas the frame structure began to collapse at 700 °C and was heavily wrecked at 800 °C (Fig. 1b-1d). The Fc-C_{60} microstructures (FM) show a clean and smooth surface (Fig. 1a2) while a number of small nanoparticles appeared on the surface of FMN600 (Fig. 1b2), which can be ascribed to the agglomeration of the iron phase. At higher temperatures, hierarchically dispersed porous structures appear in FMN700 and FMN800 (Fig. 1c2-d2), providing an advantageous mass transport channel for electrochemical ORR.

For comparison, Fc-C_{60} powder (FP) was directly heated at 700 °C under NH_3 (the obtained sample was named FPN700), and Fc-C_{60} microstructure (FM) was annealed at 700 °C under Ar (the obtained sample was named FMA700), respectively. FPN700 displayed irregular morphology and no trace of pores or nanoparticles can be distinguished (Fig. S3a1-a2). FMA700 showed the non-porous microstructures with Fe_3O_4 nanoparticles larger than 100 nm (Fig. S3b1-b2 and Fig. S4). By comparing the morphologic structures of FPN700, FMA700 and FMN700, the positive effects of the LLIP process and NH_3 etching function on pore generation and metal aggregation inhibition were demonstrated.

The micro-morphologies of the prepared samples were also examined by TEM and HRTEM (Fig. 2). The FM sample shows smooth surfaces and edges (Fig. 2a1). After high-temperature treatment in NH_3, the FMN600/700/800 samples present irregular edges and a number of nanoparticles (Fig. 2b1, c1 and d1). Moreover, hollow domains and pores became dominant with the increase of temperature, suggesting the effective etching effect of NH_3. At a relatively low temperature of 600 °C, the Fe_3O_4 nanoparticles ranging from 8 to 20 nm were found wrapped in carbon sheets over seven layers and uniformly distributed on FMN600 (Fig. 2b1-b2). The FMN700 and FMN800 samples present a series of open pores and more exposed and larger nanoparticles with the size of about 17 ~ 50 nm in FMN700 and more than 160 nm in FMN800 (Fig. 2c1-c2, d1-d2). Unexpectedly, the FMN700 displays the stacking of short-range ordered nanographenes (interlayer spacing of 4.1 ~ 4.8 Å) derived from the fullerene fragments (Fig. 2c2 and Fig. S5a), which can facilitate the transportation of the oxygen molecules (kinetic diameter ≈ 3.46 Å) to the active sites.[46-48] Combined with the favorable porous structure of the obtained samples, a solid foundation has been established for high-performance ORR. The SEM, TEM and HRTEM images of the cuboid structure show the same porous features and uniform Fe_3O_4 nanoparticles as the microplates (Fig. S5b,c,d). The above observations confirmed the homogeneous phase distributions on the cuboid and microplate.

The high-resolution transmission electron microscopy (HRTEM) images and the corresponding Fourier transformation were displayed in Fig. 2a2–2d2. FM shows lattice fringe image with the measured lattice plane distance of 1.01 nm (Fig. 2a2). For FMN600, FMN700 and FMN800 (Fig. 2b2–d2), the measured lattice plane distances of 0.25, 0.30 and 0.48 correspond to the (311), (220) and (111) lattice planes of

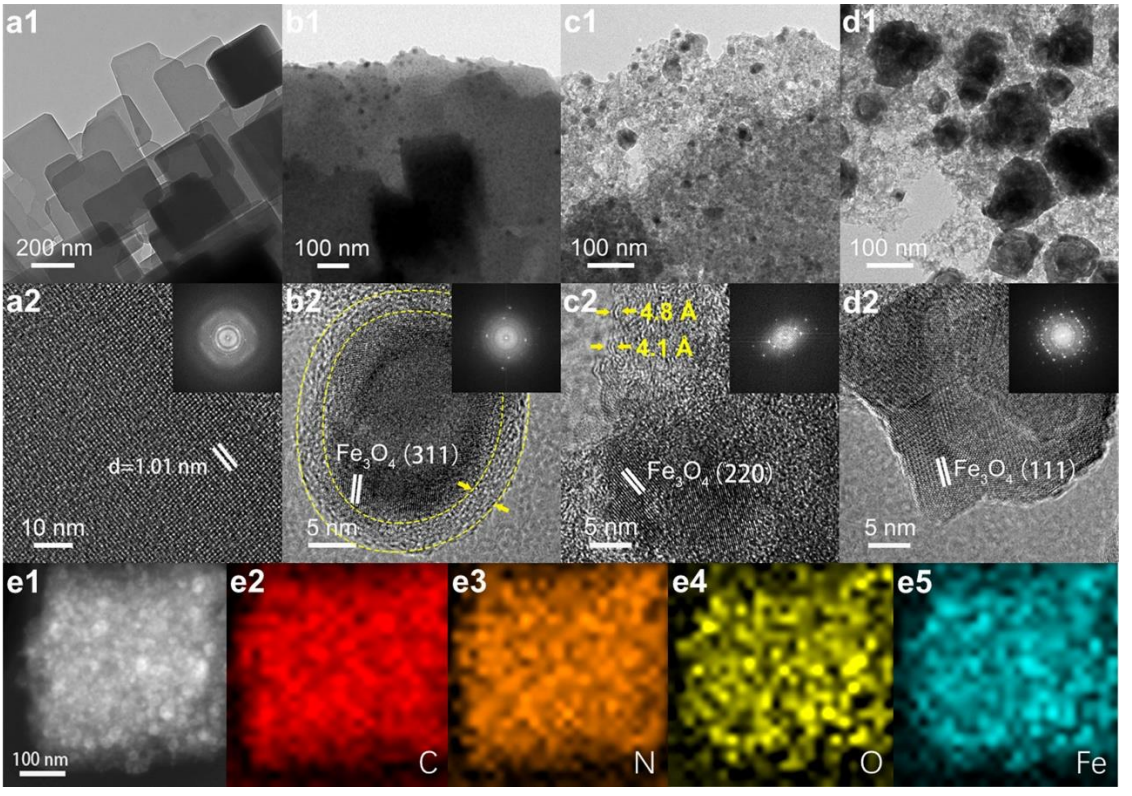

Fig. 2 TEM and HRTEM images of FM (a1, a2), FMN600 (b1, b2), FMN700 (c1, c2) and FMN800 (d1, d2), HAADF-STEM image of the selected area of FMN700 (e1) and the corresponding EDX elemental mapping of C (e2), N (e3), O (e4), Fe (e5).

Fe_3O_4, respectively.[49] High-angle annular dark field scanning transmission electron microscopy (HAADF-STEM) of FMN700 revealed heterogeneous contrast because of the abundant pore structures within the carbon framework (Fig. 2e1). The corresponding energy dispersive X-ray (EDX) elemental mapping images demonstrated the uniform distribution of C, N, O, and Fe (Fig. 2e2–e5).

To understand the phase structures of the fullerene-derived materials, X-ray powder diffraction (XRD) was performed as depicted in Fig. 3a and Fig. S6. The FM sample shows well-defined diffraction peaks, indicating the FM microstructure is highly crystalline (Fig. S6). After annealing at 600, 700 and 800 °C under NH_3 stream, the peaks of FM sample gradually faded out until one peak at about 20° was left. This broad diffraction peak at about 20° in FMN700 corresponds to the short-range ordered nanographene phase with the interlayer spacing of d = 4.4 Å, which is from the decomposition of the Fc-C_{60} microstructure (Fig. 2c2). The broadened interlayer spacing is larger than that of graphite (d = 3.4 Å) and beneficial for the diffusion of oxygen molecules to the active sites.[48] At high temperature of 800 °C, a broad and weak peak at about 24° was observed owing to the stacking of graphene sheets. The newly formed peaks at 2θ = 30°, 35.5°, 43°, 53.5°, 57° and 63° correspond to the (220), (311), (400), (422), (511) and (440) lattice planes of Fe_3O_4 phase, respectively (JCPDS no. 65-3107). The diffraction peaks of the Fe_3O_4 phase become more distinct in FMN800, implying the aggregation of the metal phase by rising temperatures.

Raman spectroscopy was employed to further analyze the structures of the synthesized materials in Fig. 3b. The FM sample shows seven characteristic vibration bands of fullerene C_{60} corresponding to Ag(1) breathing mode at 491 cm^{-1}, Ag(2) pentagonal pinch mode at 1461 cm^{-1} and five Hg bands at 431, 711, 773, 1427 and 1567 cm^{-1} (labeled with star), respectively.[50] After annealing under NH_3, two significant bands at ~ 1336 and ~ 1599 cm^{-1} for D- and G-band, respectively were obtained for FPN700, FMA700, FMN600, FMN700 and FMN800, which confirmed the decomposition of the fullerene molecules into the defected graphitic carbon. The intensity ratio of D-band and G-band (I_D/I_G) is generally indexed as the disordered nature of carbon materials. The I_D/I_G values of FMN600, FMN700 and FMN800 increases from 0.76, 0.85 to 0.89, implying more defect density on the carbon structures upon the rising of temperature. The I_D/I_G values of FPN700 and FMA700 are 0.92 and 0.88, respectively (Fig. 3b), higher than FMN700 (0.85), which indicates that the LLIP process and NH_3-activation contribute to enhance the degree of graphitization by reacting NH_3 with the amorphous carbons to generate gaseous hydrocarbons.[42,45,51-52] The broad peak from 2400 to 3200 cm^{-1} was typically caused by the 2D band from few-layer graphene sheets and D + D′ from the defects, suggesting the emerging of few-layer graphene domains and exposed edges and defects under annealing conditions.[53]

Nitrogen adsorption/desorption characterizations were carried out to examine the specific surface area (SSA) and pore size distributions of the prepared samples (Fig. 3c). Based on BET simulation, the specific SSA of FM, FPN700, FMA700, FMN600, FMN700 and FMN800 are 6.9, 419.8, 353.8, 372.1,

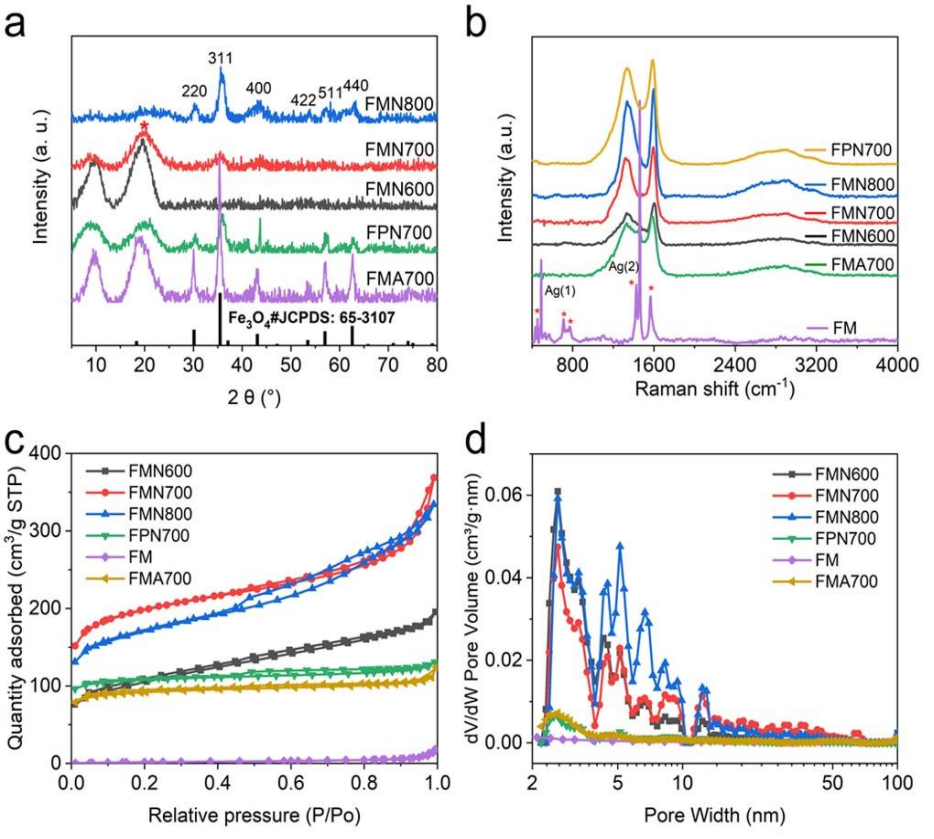

Fig. 3. (a) XRD patterns of FMA700, FPN700, FMN600, FMN700 and FMN800, (b) Raman spectra of FM, FPN700, FMA700, FMN600, FMN700 and FMN800, c) N_2 adsorption/desorption isotherms and (d) pore size distribution of the FM, FPN700, FMA700, FMN600, FMN700 and FMN800.

733.1 and 622.7 m^2 g^{-1}, respectively and the average pore volumes are 0.029, 0.202, 0.180, 0.302, 0.571 and 0.518 cm^3 g^{-1}, respectively. It can be seen that the NH_3 plays a critical role in increasing the SSA and pore volumes. The appearance of hysteresis loops (Fig. 3c) confirmed the mesoporous structures of FPN700 and FMN600/700/800 due to the NH_3 activation process. Furthermore, the SSA and pore volume of FMN700 are much higher than those of FPN700 and FMA700, which further proved the positive effects of the assembly process and NH_3 function. The pore size distribution plots obtained by the NLDFT method in Fig. 3d depicted the wide aperture distribution with pore width ranging from a few to tens of nanometers, which benefits the mass transport during electrochemical processes. The high SSA and hierarchical pore size distribution of FMN700 provide imperative foundations for ORR performance.

X-ray photoelectron spectroscopy (XPS) was adapted to determine the elemental composition and chemical state of the obtained samples, as displayed in Fig. 4, Fig. S7, S8 and S9. The elemental weight ratio listed in Table. S1 presents that the FMN700 achieved a N content of 1.6 wt.%, whereas the FMA700 has much lower N content of 0.7 wt. %, which means that the introduction of NH_3 resulted in the increase of N content. The high-resolution spectra of Fe 2p (Fig. 4a) present characteristic peaks at 710.5, 713.5, 723.3 and 725.5 eV corresponding to Fe $2P_{1/2}$, Fe $2P_{3/2}$ and Fe oxides accompanied by a satellite peak at 718.5 eV.[54,55] The high-resolution C 1s spectra (Fig. 4b) give characteristic peaks at 284.5, 285.2 286.5, and 288.8 eV, corresponding to the sp^2 hybrid C–C, C=N&C–O, C=O&C–N and O–C=O, respectively.[43] The formation of C-O and C=O are possibly ascribed to the absorbed ethanol used in the LLIP process. The O 1s spectra exhibit three peaks at 530.2, 531.9 and 533.2 eV corresponding to O–Fe, O=C and O–C, respectively (Fig. S7).[56] The chemical state of nitrogen becomes interesting as the electrochemical behavior can dramatically change upon the introduction of different nitrogen functional groups. The N 1s high-resolution spectra of FMN700 and FPN700 can be deconvoluted into pyridinic N (398.5 eV), pyrrolic N (399.4 eV) and graphitic N (400.8 eV), respectively (Fig. 4c and Fig. S9), while the graphitic N was not observed in FMA700 (Fig. S8c). The relative contents of pyrrolic N and pyridinic N showed a downward trend from FMN600, FMN700 to FMN800, while graphitic N increased with the elevated temperatures because of its higher stability. Compared with FMN600 and FPN700, FMN700 has higher pyridine and graphite N content, and these two kinds of N have been proved to be beneficial for electrochemical ORR performance.[43,45] The XPS results corroborate that control of the annealing temperature and atmosphere can effectively change the contents of the pyrrolic N, pyridinic N and graphitic N of the fullerene-derived materials (Fig. 4d).[57,58]

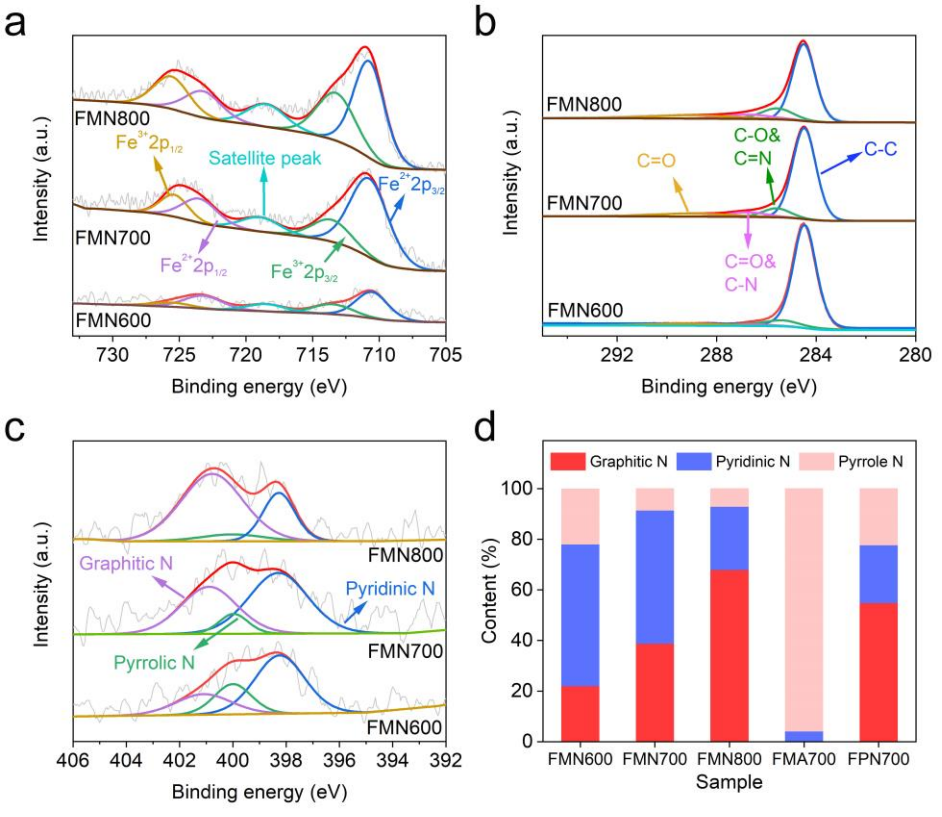

Fig. 4. High resolution XPS spectra of Fe 2p (a), C 1s (b) and N 1s (c) for FMN600, FMN700 and FMN800. (d) The nitrogen composition of FMN600, FMN700, FMN800, FMA700 and FPN700.

Electrochemical characterizations are conducted to examine the ORR activity of the obtained samples. Fig. 5a shows the cyclic voltammetry (CV) curves of the Fc-C_{60}-derived materials and Pt/C sample. Among the Fc-C_{60}-derived samples, FMN700 showed the most positive oxygen reduction peak at 0.803 V vs. RHE. Fig. 5b presents the linear sweep voltammetry (LSV) profiles of the samples in O_2-saturated 0.1 M KOH at 1600 rpm. FMN700 presented the largest onset

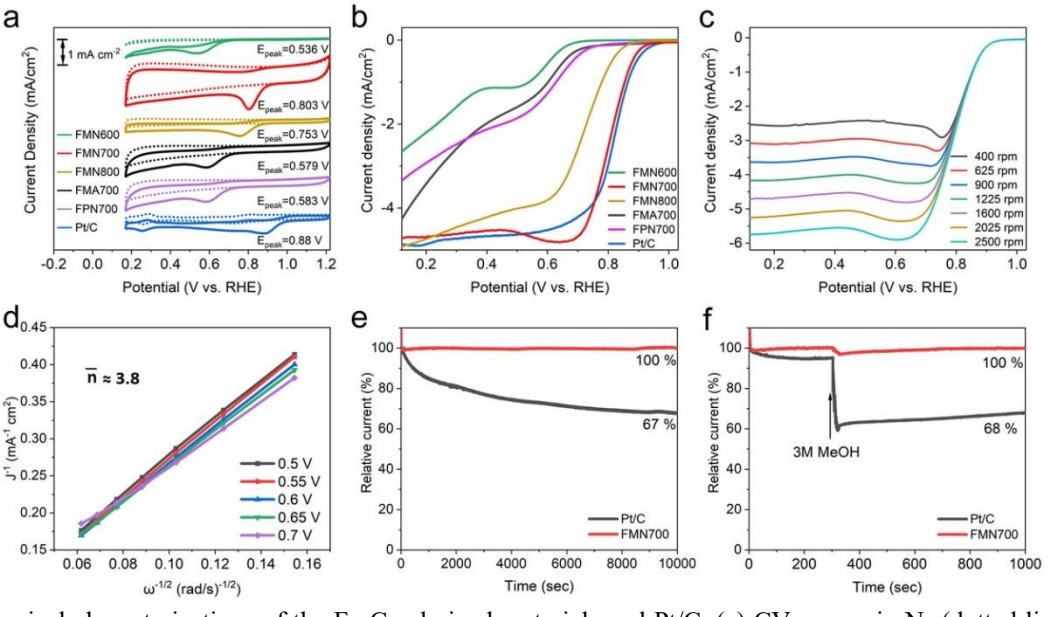

Fig. 5 Electrochemical characterizations of the Fc-C_{60}-derived materials and Pt/C. (a) CV curves in N_2 (dotted line) and O_2 (solid line) saturated 0.1 M KOH solution (scanning rate: 10 mV s^{-1}). (b) LSV curves of different samples at 1600 rpm in O_2 saturated 0.1 M KOH (scanning rate: 10 mV s^{-1}). (c) LSV curves of FMN700 in O_2 saturated 0.1 M KOH at different rotating speeds (scanning rate: 10 mV s^{-1}). (d) Electron transfer numbers of FMN700 calculated based on K-L plots. (e) The stability and (f) methanol-tolerance evaluation of FMN700 and Pt/C tested by the current-time chronoamperometric responses at 0.6 V versus RHE.

Table 1 Comparison of the ORR performances of nanocarbons derived from fullerene and Fe-doped carbon materials.

Samples	E_{on} (V vs. RHE)	$E_{1/2}$ (V vs. RHE)	Mass loading (mg cm^{-2})	Electrolyte	ref.
FMN700	0.93	0.81	0.5	0.1 M KOH	This work
C_{60}-derived pentagon carbon	/	0.78	0.4	0.1 M KOH	32
MFC_{60}-130	0.82	0.76	/	0.5 M KOH	35
MFC_{70}-150	0.86[#]	0.75[#]	/	0.1 M KOH	36
Cu(15%)-MFC_{60}	0.86	0.76	0.153	0.1 M KOH	37
Graphene–C_{60} hybrid	0.8[#]	/	0.05	0.1 M KOH	33
Fe-MFC_{60}	0.85	0.78	0.285	0.5 M KOH	40
Fe-N/C-700	0.910	0.821	0.51	0.1 M NaOH	59
HNCS71	0.97	0.82	0.5	0.1 M KOH	60
Fe–N–CB	0.849	0.746	0.9	0.1 M KOH	61
$(FeP)_n$-CNT hybrid	0.88	0.76	0.51	0.1 M KOH	62
Fe@FeNx/NC	0.96	0.82	0.4	0.1 M KOH	63
Fe_{AS}-NC-12	0.97	0.87	0.250	0.1 M KOH	64
Fe@S,N-DC	0.99	0.88	1.0	0.1 M KOH	65

[#] Potentials (vs. Ag/AgCl) were converted to values (vs. RHE) by the Nernst equation.[66]

potential (E_{on}) of 0.93 V and half-wave potential ($E_{1/2}$) of 0.81 V, which are comparable to those of Pt/C. Whereas, FPN700 and FMA700 delivered low E_{on} and $E_{1/2}$, and dilatory current response below 0.6 V vs. RHE, which verified that the LLIP process and the introduction of NH_3 are essential to improve the performance of FMN700, thereby boosting the sluggish ORR. To provide a more specific view, ORR performances of the relevant materials measured by onset potential and half-wave potential were listed in Table. 1. The FMN700 in this work gives the higher E_{on} and $E_{1/2}$ among the fullerene-based nanocarbons and is quite competitive with the other remarkable Fe/C composites.

Fig. 5c and Fig. S10 showed the LSV curves of Fc-C_{60}-derived materials at rotating speeds from 400 to 2500 rpm in O_2-saturated 0.1 M KOH. Compared to other samples, FMN700 presented the highest limiting current density of 5.7 mA cm^{-2} at 2500 rpm. The Koutecky–Levich plots of FMN700 displayed nearly linear and parallel lines (Fig. 5d). The average electron transfer number ($\bar{n}$) was calculated to be 3.8 in the potential range of 0.55–0.7 V, implying the high selectivity towards a one-step four-electron pathway. Furthermore, the FMN700 showed outstanding stability and poison tolerance with methanol. Whereas the referenced commercial Pt/C severely decayed to 68% of the initial current (Fig. 5e, f).

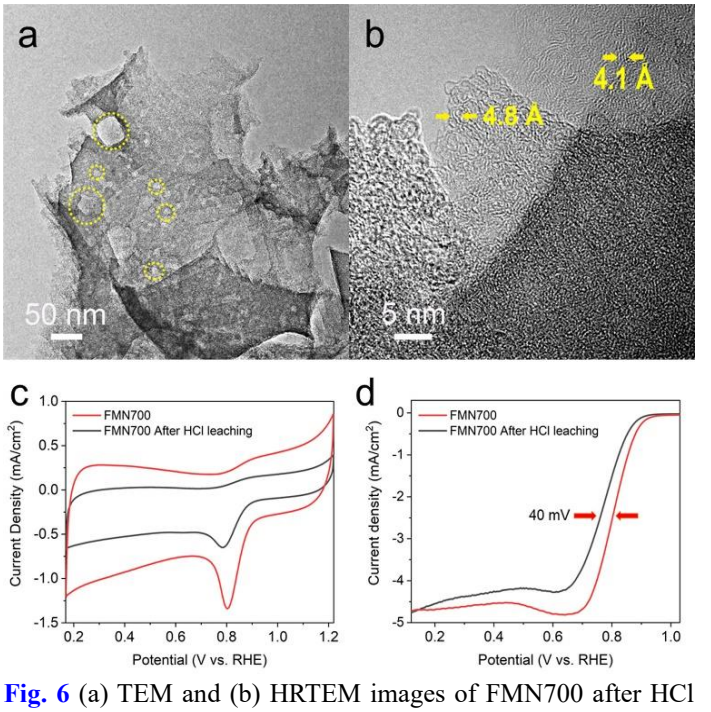

Fig. 6 (a) TEM and (b) HRTEM images of FMN700 after HCl leaching, (c) CV and (d) LSV curves of FMN700 before and after HCl leaching in O_2 saturated 0.1 M KOH (scanning rate: 10 mV s^{-1}).

To verify the effect of Fe_3O_4 nanoparticles on the ORR activity, FMN700 was etched with 1 M HCl for 8 hours to remove the Fe_3O_4 nanoparticles. TEM image of the treated sample revealed only hollow pits (yellow circles in Fig. 6a) instead of Fe_3O_4 nanoparticles on the carbon framework. HRTEM image in Fig. 6b showed that the short range ordered nanographene with the interlayer spacing of 4.1 ~ 4.8 Å was remained. The oxygen reduction peaks in the CV curves decreased from the initial 0.803 V (FMN700) to 0.783 V (Fig. 6c), and the $E_{1/2}$ value showed a 40 mV attenuation after the removal of Fe_3O_4 nanoparticles (Fig. 6d). The Fe_3O_4 nanoparticles on the 3D porous carbon framework have a

synergetic effect for the enhanced ORR activity. Thus, the excellent ORR performance of FMN700 is ascribed to the synergistic effects of large surface area, hierarchical pore structures, short-range ordered nanographene, favorable nitrogen doping and the uniform Fe_3O_4 active sites.

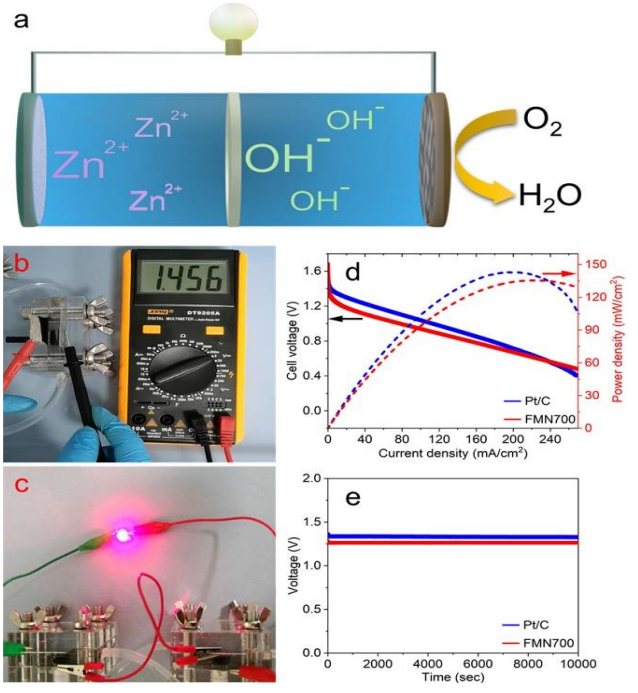

Fig. 7 (a) Schematic configuration of the Zn-air battery device. (b) Open circuit voltage of Zn-air battery using FMN700 as the cathode. (c) Photograph of a red LED lighted by two Zn-air batteries connected in series. (d) Discharge polarization curves and corresponding power density of Zn-air batteries with FMN700 and 20 wt% Pt/C catalysts, respectively. (e) Galvanostatic discharge curves of FMN700 and 20 wt% Pt/C at a current density of 10 mA cm^{-2} for 10000 s.

The electrochemical performance of FMN700 was further examined by applying FMN700 as an air cathode in a Zn-air battery device with 6 M KOH as the electrolyte (Fig. 7a). The device presents an open circuit voltage as high as 1.456 V (Fig. 7b). A 1.8 V red LED can be lit by two Zn-air batteries connected in series (Fig. 7c). The polarization curves and the corresponding power density plots of Zn-air batteries with FMN700 and 20% Pt/C were depicted in Fig. 7d. At 0.6 V, FMN700 catalyst exhibited a high current density of 223.6 mA cm^{-2} with a power density of 135.5 mW cm^{-2}, which is comparable to 142.9 mW cm^{-2} of Pt/C and much higher than 111.4 mW cm^{-2} of the fullerene C_{60}-derived carbon.[32] The galvanostatic discharge tests of the assembled Zn−air battery at the current density of 10 mA cm^{-2} for 10000 s revealed the long-term stability (Fig. 7e). Remarkably, the battery with FMN700 cathode shows a potential of 1.26 V at 10 mA cm^{-2} close to 1.34 V of Pt/C catalyst.

4. Conclusions

In summary, a fullerene derivative was introduced as a precursor for synthesis of active ORR catalyst. Pyrolysis of the fullerene derivative microstructures under an NH_3 atmosphere was conducted to prepare Fe_3O_4/N-C porous nanomaterials. The obtained FMN700 has developed multiple merits, including large surface area, favorable N doping, the short-range ordered nanographene and advantageous Fe_3O_4 nanoparticles, which can boost the oxygen reduction. Under these synergetic effects, FMN700 shows high onset potential (0.93 V) and half-wave potential (0.81 V), along with excellent durability and methanol tolerance. And delivered the high power density of zinc-air battery. The utilization of fullerene host-dopant synergism is proved to be a practical way for enhancing ORR performance. It can be concluded that control of fullerene structures by covalently bonding required units can effectively adjust their catalytic properties. This work not only provides an understanding of the NH_3-assisted pyrolysis behavior of fullerene materials but also presents a novel perspective for the preparation of new catalysts from fullerene molecules for the wide applications.

Acknowledgements

The financial supports from National Natural Science Foundation of China (Grant No. 21971077, 22071070) and the Graduates' Innovation Fund, Huazhong University of Science and Technology (No. 2020yjsCXCY029) are gratefully acknowledged. The authors thank the facility support of the Center for Nanoscale Characterization & Devices (CNCD), WNLO of HUST and the Analytical and Testing Center in Huazhong University of Science and Technology for all related measurements.

Supporting information

Applicable

Conflict of interest

There are no conflicts to declare.

References

[1] W. Wang, Q. Jia, S. Mukerjee, S. Chen, *ACS Catal.,* 2019, **9**, 10126-10141, doi: 10.1021/acscatal.9b02583.

[2] H. Wan, A. W. Jensen, M. Escudero-Escribano, J. Rossmeisl, *ACS Catal.,* 2020, **10**, 5979-5989, doi: 10.1021/acscatal.0c01085.

[3] Y. Zhan, F. Xie, H. Zhang, Y. Jin, H. Meng, J. Chen, X. Sun, *ACS Appl. Mater. Interfaces,* 2020,**12**, 17481-17491, 10.1021/acsami.0c00126.

[4] H. A. Gasteiger, S. S. Kocha, B. Sompalli, F. T. Wagner, *Appl. Catal., B,* 2005, **56**, 9-35, doi: 10.1016/j.apcatb.2004.06.021.

[5] C. Chen, Y. Kang, Z. Huo, Z. Zhu, W. Huang, H. L. Xin, J. D. Snyder, D. Li, J. A. Herron, M. Mavrikakis, M. Chi, K. L. More, Y. Li, N. M. Markovic, G. A. Somorjai, P. Yang, V. R. Stamenkovic, *Science,* 2014, **343**, 1339, 10.1126/science.1249061.

[6] T. Bian, H. Zhang, Y. Jiang, C. Jin, J. Wu, H. Yang, D. Yang, *Nano Lett.,* 2015, **15**, 7808-7815, doi: 10.1021/acs.nanolett.5b02960.
[7] J. Wang, Z. Huang, W. Liu, C. Chang, H. Tang, Z. Li, W. Chen, C. Jia, T. Yao, S. Wei, Y. Wu, Y. Li, *J. Am. Chem. Soc.,* 2017,**139**, 17281-17284, doi: 10.1021/jacs.7b10385.
[8] K. Strickland, E. Miner, Q. Jia, U. Tylus, N. Ramaswamy, W. Liang, M. T. Sougrati, F. Jaouen, S. Mukerjee, *Nat. Commun.,* 2015, **6**, 7343, doi: 10.1038/ncomms8343.
[9] L. Yang, S. Jiang, Y. Zhao, L. Zhu, S. Chen, X. Wang, Q. Wu, J. Ma, Y. Ma, Z. Hu, *Angew. Chem., Int. Ed.,* 2011, **50**, 7132-7135, doi: 10.1002/anie.201101287.
[10] Y. Zhao, L. Yang, S. Chen, X. Wang, Y. Ma, Q. Wu, Y. Jiang, W. Qian, Z. Hu, *J. Am. Chem. Soc.,* 2013,**135**, 1201-1204, doi: 10.1021/ja310566z.
[11] X. Liu, L. Dai, *Nat. Rev. Mater.,* 2016, **1**, 16064, doi: 10.1038/natrevmats.2016.64.
[12] Y. Jia, L. Zhang, L. Zhuang, H. Liu, X. Yan, X. Wang, J. Liu, J. Wang, Y. Zheng, Z. Xiao, E. Taran, J. Chen, D. Yang, Z. Zhu, S. Wang, L. Dai, X. Yao, *Nat. Catal.,* 2019,**2**, 688-695, doi: 10.1038/s41929-019-0297-4.
[13] J. Niu, R. Shao, M. Liu, Y. Zan, M. Dou, J. Liu, Z. Zhang, Y. Huang, F. Wang, *Adv. Funct. Mater.,* 2019,**29**, 1905095, doi: 10.1002/adfm.201905095.
[14] Y. Jiang, L. Yang, T. Sun, J. Zhao, Z. Lyu, O. Zhuo, X. Wang, Q. Wu, J. Ma, Z. Hu, *ACS Catal.,* 2015, **5**, 6707-6712, doi: 10.1021/acscatal.5b01835.
[15] Z. S. Wu, S. Yang, Y. Sun, K. Parvez, X. Feng, K. Mullen, *J. Am. Chem. Soc.,* 2012, **134**, 9082-9085, doi: 10.1021/ja3030565.
[16] S. Gao, B. Fan, R. Feng, C. Ye, X. Wei, J. Liu, X. Bu, *Nano Energy,* 2017, **40**, 462-470, doi: 10.1016/j.nanoen.2017.08.044.
[17] Z. Li, G. Li, L. Jiang, J. Li, G. Sun, C. Xia, F. Li, *Angew. Chem., Int. Ed.,* 2015, **54**, 1494-1498, doi: 10.1002/anie.201409579.
[18] J. Duan, S. Chen, S. Dai, S. Z. Qiao, *Adv. Funct. Mater.,* 2014, **24**, 2072-2078, doi: 10.1002/adfm.201302940.
[19] X. Ge, A. Sumboja, D. Wuu, T. An, B. Li, F. W. T. Goh, T. S. A. Hor, Y. Zong, Z. Liu, *ACS Catal.,* 2015,**5**, 4643-4667, doi: 10.1021/acscatal.5b00524.
[20] X. Li, B. Y. Guan, S. Gao, X. W. Lou, *Energy Environ. Sci.,* 2019, **12**, 648-655, doi: 10.1039/C8EE02779J.
[21] F. Deganello, D. N. Oko, M. L. Testa, V. La Parola, M. L. Tummino, C. O. Soares, J. G. Rivera, G. Orozco, D. Guay, A. C. Tavares, *ACS Appl. Energy Mater.,* 2018, **1**, 2565-2575, doi: 10.1021/acsaem.8b00282.
[22] S. Fu, C. Zhu, J. Song, M. H. Engelhard, H. Xia, D. Du, Y. Lin, *ACS Appl. Mater. Interfaces,* 2016, **8**, 35213-35218, doi: 10.1021/acsami.6b11537.
[23] X. Wan, X. Liu, Y. Li, R. Yu, L. Zheng, W. Yan, H. Wang, M. Xu, J. Shui, *Nat. Catal,* 2019, **2**, 259-268, doi: 10.1038/s41929-019-0237-3.
[24] E. Hu, X.-Y. Yu, F. Chen, Y. Wu, Y. Hu, X. W. Lou, *Adv. Energy Mater.,* 2017, **8**, 1702476, doi: 10.1002/aenm.201702476.
[25] J. Coro, M. Suárez, L. S. R. Silva, K. I. B. Eguiluz, G. R. Salazar-Banda, *Int. J. Hydrogen Energy,* 2016, **41**, 17944-17959, doi: 10.1016/j.ijhydene.2016.08.043.
[26] T. Xu, W. Shen, W. Huang, X. Lu, *Mater. Today Nano,* 2020, 100081, doi: 10.1016/j.mtnano.2020.100081.
[27] F. Gao, G. L. Zhao, S. Yang, J. J. Spivey, *J. Am. Chem. Soc,* 2013, **135**, 3315-3318, doi: 10.1021/ja309042m.
[28] X. Chen, J. Chang, Q. Ke, *Carbon,* 2018, **126**, 53-57, doi: 10.1016/j.carbon.2017.10.007.
[29] S. H. Noh, C. Kwon, J. Hwang, T. Ohsaka, B. J. Kim, T. Y. Kim, Y. G. Yoon, Z. Chen, M. H. Seo, B. Han, *Nanoscale,* 2017,**9**, 7373-7379, doi: 10.1039/c7nr00930e.
[30] K. Mao, W. Zhang, J. Dai, X. C. Zeng, *Nanoscale,* 2019,**11**, 19422-19428, doi: 10.1039/c9nr05338g.
[31] Y. Wang, M. Jiao, W. Song, Z. Wu, *Carbon,* 2017,**114**, 393-401, doi: 10.1016/j.carbon.2016.12.028.
[32] J. Zhu, Y. Huang, W. Mei, C. Zhao, C. Zhang, J. Zhang, I. S. Amiinu, S. Mu, *Angew. Chem., Int. Ed.,* 2019, **58**, 3859-3864, doi: 10.1002/anie.201813805.
[33] J. Guan, X. Chen, T. Wei, F. Liu, S. Wang, Q. Yang, Y. Lu, S. Yang, *J. Mater. Chem. A,* 2015, **3**, 4139-4146, doi: 10.1039/c4ta05456c.
[34] T. Xu, D. Yu, Z. Du, W. Huang, X. Lu, *Chem. - Eur. J.,* 2020, **26**, 10811-10816, doi: 10.1002/chem.202001404.
[35] M. R. Benzigar, S. Joseph, H. Ilbeygi, D. H. Park, S. Sarkar, G. Chandra, S. Umapathy, S. Srinivasan, S. N. Talapaneni, A. Vinu, *Angew. Chem., Int. Ed.,* 2018, **57**, 569-573, doi: 10.1002/anie.201710888.
[36] M. R. Benzigar, S. Joseph, A. V. Baskar, D.-H. Park, G. Chandra, S. Umapathy, S. N. Talapaneni, A. Vinu, *Adv. Funct. Mater.,* 2018, **28**, 1803701, doi: 10.1002/adfm.201803701.
[37] G. Saianand, A. I. Gopalan, J. C. Lee, C. I. Sathish, K. Gopalakrishnan, G. E. Unni, D. Shanbhag, V. Dasireddy, J. Yi, S. Xi, A. H. Al-Muhtaseb, A. Vinu, *Small,* 2020, **16**, e1903937, doi: 10.1002/smll.201903937.
[38] F. Caporossi, B. Floris, P. Galloni, E. Gatto, M. Venanzi, *Eur. J. Inorg. Chem.,* 2006, **2006**, 4362-4366, doi: 10.1002/ejoc.200600318.
[39] E. Bae, N. D. Kim, B. K. Kwak, J. Park, J. Lee, Y. Kim, K. Choi, J. Yi, *Carbon,* 2010, **48**, 3676-3681, doi: 10.1016/j.carbon.2010.06.007.
[40] M. R. Benzigar, S. Joseph, G. Saianand, A.-I. Gopalan, S. Sarkar, S. Srinivasan, D.-H. Park, S. Kim, S. N. Talapaneni, K.

Ramadass, A. Vinu, *Micropor. Mesopor. Mat.,* 2019, **285**, 21-31, doi: 10.1016/j.micromeso.2019.04.071.
[41] Z. Peng, Y. Hu, J. Wang, S. Liu, C. Li, Q. Jiang, J. Lu, X. Zeng, P. Peng, F. F. Li, *Adv. Energy Mater.,* 2019,**9**, 1802928, 10.1002/aenm.201802928.
[42] T.-N. Tran, C.-H. Shin, B.-J. Lee, J. S. Samdani, J.-D. Park, T.-H. Kang, J.-S. Yu, *Catal. Sci. Technol.,* 2018, **8**, 5368-5381, doi: 10.1039/c8cy01140k.
[43] Y. Su, H. Jiang, Y. Zhu, X. Yang, J. Shen, W. Zou, J. Chen, C. Li, *J. Mater. Chem. A,* 2014, **2**, 7281-7287, doi: 10.1039/c4ta00029c.
[44] J. Wu, Z. Pan, Y. Zhang, B. Wang, H. Peng, *J. Mater. Chem. A,* 2018, **6**, 12932-12944, doi: 10.1039/C8TA03968B.
[45] H. Meng, N. Larouche, M. Lefèvre, F. Jaouen, B. Stansfield, J.-P. Dodelet, *Electrochim. Acta,* 2010, **55**, 6450-6461, doi: 10.1016/j.electacta.2010.06.039.
[46] A. B. Shelekhin, A. G. Dixon, Y. H. Ma, *AIChE J.,* 1995,**41**, 58-67, doi: 10.1002/aic.690410107.
[47] Y. Wang, R. T. Yang, *ACS Sustain. Chem. Eng.,* 2019,**7**, 3301-3308, doi: 10.1021/acssuschemeng.8b05339.
[48] S. Chen, N. Zhang, C. W. Narváez Villarrubia, X. Huang, L. Xie, X. Wang, X. Kong, H. Xu, G. Wu, J. Zeng, H.-L. Wang, *Nano Energy,* 2019, **66**, 104164, doi: 10.1016/j.nanoen.2019.104164.
[49] C. Lian, Z. Wang, R. Lin, D. Wang, C. Chen, Y. Li, *Nano Res.,* 2017,**10**, 3303-3313, doi: 10.1007/s12274-017-1543-8.
[50] K. Vimalanathan, R. G. Shrestha, Z. Zhang, J. Zou, T. Nakayama, C. L. Raston, *Angew. Chem., Int. Ed.,* 2017,**129**, 8518-8521, doi: 10.1002/ange.201608673.
[51] A. Moisala, A. G. Nasibulin, D. P. Brown, H. Jiang, L. Khoiriachtchev, E. I. Kauppinen, *Chem. Eng. Sci.,* 2006,**61**, 4393-4402, doi: 10.1016/j.ces.2006.02.020.
[52] X. Li, H. Wang, J. T. Robinson, H. Sanchez, G. Diankov, H. Dai, *J. Am. Chem. Soc.,* 2009, **131**, 15939-15944, doi: 10.1021/ja907098f.
[53] A. C. Ferrari, D. M. Basko, *Nat. Nanotechnol.,* 2013,**8**, 235-246, doi: 10.1038/nnano.2013.46.
[54] Y. Liu, Y. Fu, L. Liu, W. Li, J. Guan, G. Tong, *ACS Appl. Mater. Interfaces,* 2018, **10**, 16511-16520, doi: 10.1021/acsami.8b02770.
[55] K. Srinivas, Y. Chen, B. Wang, B. Yu, X. Wang, Y. Hu, Y. Lu, W. Li, W. Zhang, D. Yang, *ACS Appl. Mater. Interfaces,* 2020, **12**, 31552-31563, doi: 10.1021/acsami.0c09737.
[56] X. Wang, X. Huang, Z. Chen, X. Liao, C. Liu, B. Shi, *J. Mater. Chem. C,* 2015,**3**, 10146-10153, doi: 10.1039/c5tc02689j.
[57] Z. Tan, K. Ni, G. Chen, W. Zeng, Z. Tao, M. Ikram, Q. Zhang, H. Wang, L. Sun, X. Zhu, X. Wu, H. Ji, R. S. Ruoff, Y. Zhu, *Adv. Mater.,* 2017,**29**, 1603414, doi: 10.1002/adma.201603414.
[58] Z. Chen, K. Mou, S. Yao, L. Liu, *J. Mater. Chem. A,* 2018, **6**, 11236-11243, doi: 10.1039/c8ta03328e.
[59] Y. Liu, J. Ruan, S. Sang, Z. Zhou, Q. Wu, *Electrochim. Acta,* 2016, **215**, 388-397, doi: 10.1016/j.electacta.2016.08.090.
[60] H. Wang, W. Wang, Y.Y. Xu, S. Dong, J. Xiao, F. Wang, H. Liu, B.Y. Xia, *ACS Appl. Mater. Interfaces,* 2017,**9**, 10610-10617, doi: 10.1021/acsami.6b15392.
[61] Y. Zhu, B. Zhang, D. W. Wang, D. S. Su, *ChemSusChem,* 2015,**8**, 4016-4021, doi: 10.1002/cssc.201501141.
[62] H. Jia, Z. Sun, D. Jiang, S. Yang, P. Du, *Inorg. Chem. Front.,* 2016, **3**, 821-827, doi: 10.1039/C5QI00198F.
[63] Y. Chen, Z. Shi, Z. Wang, C. Wang, J. Feng, B. Pang, Q. Sun, L. Yu, L. Dong, *J. Alloys Compd.,* 2020, **829**, 154558, doi: 10.1016/j.jallcom.2020.154558.
[64] T. Zhao, A. Kumar, X. Xiong, M. Ma, Y. Wang, Y. Zhang, S. Agnoli, G. Zhang, X. Sun, *ACS Appl. Mater. Interfaces,* 2020, **12**, 25832-25842, doi: 10.1021/acsami.0c04169.
[65] Y. M. Zhao, P. C. Zhang, C. Xu, X. Y. Zhou, L. M. Liao, P. J. Wei, E. Liu, H. Chen, Q. He, J. G. Liu, *ACS Appl. Mater. Interfaces,* 2020, **12**, 17334-17342, doi: 10.1021/acsami.9b20711.
[66] F. F. Abdi, R. van de Krol, *J. Phys. Chem. C,* 2012,**116**, 9398-9404, doi: 10.1021/jp3007552.

Author information

Zhiyao Peng *received his Bachelor's Degree in Materials Science and Engineering from Hubei University in 2016. He is currently a Ph.D. candidate under the supervision of Prof. Fang-Fang Li and Associate Prof. Ping Peng at Huazhong University of Science and Technology. His research interests focus on the application of fullerene-based materials in electrochemical oxygen reduction, photodetectors and supercapacitors.*

Qinglong Jiang*, currently an Assistant Professor (Tenure Track) in the Department of Chemistry and Physics in University of Arkansas, Pine Bluff. His research focuses on nanomaterials and technologies for electric-optical devices. He used to work in Argonne National Lab after his postdoc researcher career in Florida State University. He is currently serving in NASA-ASGC. 2019 DOE VFP receiver.*

Ping Peng is currently an associate professor in the State Key Laboratory of Materials Processing and Die & Mold Technology, School of Materials Science and Engineering, Huazhong University of Science and Technology. He obtained his Ph.D. in Applied Chemistry from Jilin University. His research interests mainly focus on the design and synthesis of functional carbon materials, and their applications in energy storage.

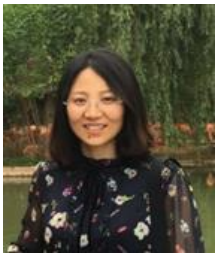

***Fangfang Li** is currently a professor at the State Key Laboratory of Materials Processing and Die & Mold Technology, School of Materials Science and Engineering, Huazhong University of Science and Technology, China. She received her Ph. D. from the Changchun Institute of Applied Chemistry, Chinese Academy of Sciences. Her research interests include fullerene chemistry, CO_2 capture and conversion, as well as synthesis of functional carbon materials for energy and catalysis applications.*

